California Winter Precipitation Change under Global Warming in the Coupled Model Intercomparison Project Phase 5 Ensemble

J. DAVID NEELIN, BAIRD LANGENBRUNNER, JOYCE E. MEYERSON, ALEX HALL, AND NEIL BERG

Department of Atmospheric and Oceanic Sciences, University of California, Los Angeles, Los Angeles, California

(Manuscript received 28 July 2012, in final form 15 January 2013)

ABSTRACT

Projections of possible precipitation change in California under global warming have been subject to considerable uncertainty because California lies between the region anticipated to undergo increases in precipitation at mid-to-high latitudes and regions of anticipated decrease in the subtropics. Evaluation of the large-scale model experiments for phase 5 of the Coupled Model Intercomparison Project (CMIP5) suggests a greater degree of agreement on the sign of the winter (December–February) precipitation change than in the previous such intercomparison, indicating a greater portion of California falling within the increased precipitation zone. While the resolution of global models should not be relied on for accurate depiction of topographic rainfall distribution within California, the precipitation changes depend substantially on large-scale shifts in the storm tracks arriving at the coast. Significant precipitation increases in the region arriving at the California coast are associated with an eastward extension of the region of strong Pacific jet stream, which appears to be a robust feature of the large-scale simulated changes. This suggests that effects of this jet extension in steering storm tracks toward the California coast constitute an important factor that should be assessed for impacts on incoming storm properties for high-resolution regional model assessments.

1. Introduction

Robust projections of future precipitation in California are limited by several factors. Along with complex topography spanning the state, the latitudinal extent of California allows for both midlatitude and subtropical atmospheric dynamics to influence the state's precipitation. This can create a dipole spatial pattern in precipitation impacts between the northern and southern portions of the state. Large-scale climate change patterns associated with global warming tend to produce reductions in precipitation in the subtropics and precipitation increases at mid-to-high latitudes, and California is located in the region between these opposing tendencies (Meehl et al. 2007). California's precipitation is also influenced by large-scale climate variability patterns such as El Niño–Southern Oscillation (ENSO) and the Pacific decadal oscillation.

To address the effects of complex topography and other locally variable effects on precipitation, a common approach is to downscale results from global models, using either high-resolution regional models or statistical relationships between large-scale meteorological factors and local precipitation. Regional models do not necessarily remove biases in stimulation of climatology; for instance, Caldwell (2010) finds that a set of regional models tends to overpredict, while large-scale models underpredict, California winter precipitation. Downscaling studies of precipitation change under global warming naturally reflect uncertainties inherited from the large scale. Mauer (2007) finds increases in wintertime precipitation over Northern California and small increases in wintertime precipitation in a Southern California basin in a statistical downscaling of 11 general circulation models (GCMs). Pierce et al. (2013) statistically downscale 16 GCM simulations and find slight wintertime precipitation increases over Northern California but decreases over Southern California. Dynamically downscaled simulations also in some cases find increases in annual and wintertime precipitation over the northern half of California (Kim 2005, Duffy

Corresponding author address: J. David Neelin, Department of Atmospheric and Oceanic Sciences, UCLA, 405 Hilgard Ave., Los Angeles, CA 90095-1565.
E-mail: neelin@atmos.ucla.edu

DOI: 10.1175/JCLI-D-12-00514.1

et al. 2006). On the other hand, Cayan et al. (2008) find reductions of precipitation on the order of 10%–20% across the region according to one GCM they analyzed. Similarly, Hayhoe et al. (2004) statistically downscale two GCMs and found general decreases in wintertime precipitation between 15% and 30%, with most reductions occurring in the Central Valley and along the north Pacific Coast. However, Cayan et al. (2008) and Kim (2005) both find increased future extreme precipitation events over Northern California.

The purpose here is to examine a regional-scale feature of Coupled Model Intercomparison Project (CMIP) phase 5 (CMIP5) model results that 1) differs from results of the previous such intercomparison, phase 3 of CMIP (CMIP3), and 2) if it could be trusted might be taken as cautiously good news for one aspect of California water resources. In examining these results from the global climate models, it must be born in mind that regional-scale features tend to be associated with high uncertainty. Not only are there issues in accuracy of precipitation simulation at the climate model grid scale in regions of strong topography, but factors arising at the large scale that affect the position and strength of such features as storm tracks can have a large impact on climate model precipitation evaluated at a local gridpoint level. However, as one moves toward the large scale, there tends to be increasing confidence in the representation of climate features in the global models, especially in terms of physical pathway. Thus in asking whether there is any basis for regarding the changes in this region in CMIP5 models as significant, we move from point-by-point assessment to examination of a relatively large-scale precipitation pattern associated with storm-track changes and the relationship of this to changes in the eastern Pacific subtropical jet. In this latter, the approach is to evaluate the region of rainfall and wind change coming onto the coast, such as would form part of the input that would be downscaled in a regional climate model. While this is a reasonable index of large-scale factors affecting California precipitation, of course it does not alone provide detailed information of the distribution of the changes within the state. We also focus on winter [December–February (DJF)] precipitation, commenting separately on possible changes in the seasonal cycle, recognizing that changes in snowpack melt evaluated in prior studies (Barnett et al. 2005; Mote et al. 2005; Barnett et al. 2008) are expected to be a robust impact on the seasonal distribution of California water resources that will interact with rainfall changes.

In this evaluation the simulations under representative concentration pathway 8.5 (RCP8.5) at the end of the century are chosen because they have a strong signal. These changes scale proportionally to global-scale temperature change (e.g., Murphy et al. 2007; Neelin et al. 2006) and so would be expected to apply with the same spatial pattern but smaller amplitude at midcentury or in concentration pathway scenarios that have lower levels of greenhouse gas, reflecting more optimistic assumptions regarding anthropogenic emissions. The RCP8.5 pathway is also very similar to the Special Report on Emissions Scenarios (SRES) A2 scenario, which is used for the CMIP3 model comparison (Moss et al. 2010).

2. West Coast precipitation changes

Figure 1 shows precipitation changes for the winter season (DJF) for the end of the century RCP8.5 scenario simulations relative to the base period (1960–90) for the West Coast of North America and the northeastern Pacific region in the CMIP5 models. To have a common grid for comparison, all models have been interpolated to a 2.5° × 2.5° latitude–longitude grid, the same resolution as the observational estimates of the Climate Prediction Center (CPC) Merged Analysis of Precipitation (CMAP; see Xie and Arkin, 1997) and the Global Precipitation Climatology Project (GPCP, version 2.2; see Huffman et al. 2001; Adler et al. 2003). The typical model resolution is approximately 2° (see Table A1 for list of models with resolutions, and complete expansions of model names). The multimodel ensemble (MME) mean is computed by first averaging all available runs for each model with multiple runs. Also shown in Fig. 1 is the climatological 3 mm day^{-1} contour as an indicator of the base period storm-track precipitation. The CMIP5 MME mean contour agrees well with that of GPCP. The CMAP contour indicates lower rainfall estimates than either of these just off the coast and along the northern edge of the storm track, but is argued to be less reliable over oceans (Yin et al. 2004). The key feature of the climatology for results here is the region off the California coast where the southern boundary of the storm track angles northeastward from about 25°N at 145°W to hit the California coast at approximately 35°N, resulting in the climatological precipitation at the California coast being smaller than at comparable latitudes in the central Pacific.

The CMIP5 MME mean precipitation change (Fig. 1a) at the large scale exhibits features that are familiar from earlier studies including CMIP3 (Meehl et al. 2007; Trenberth 2011; Scheff and Frierson 2012) models, seen in Fig. 2. Comparing to Fig. 1, features that remain qualitatively consistent include an increase in precipitation at mid-to-high latitudes and a reduction of the precipitation farther southward associated with changes in the subtropics. The latter includes a reduction in precipitation over Mexico and surrounding ocean, and

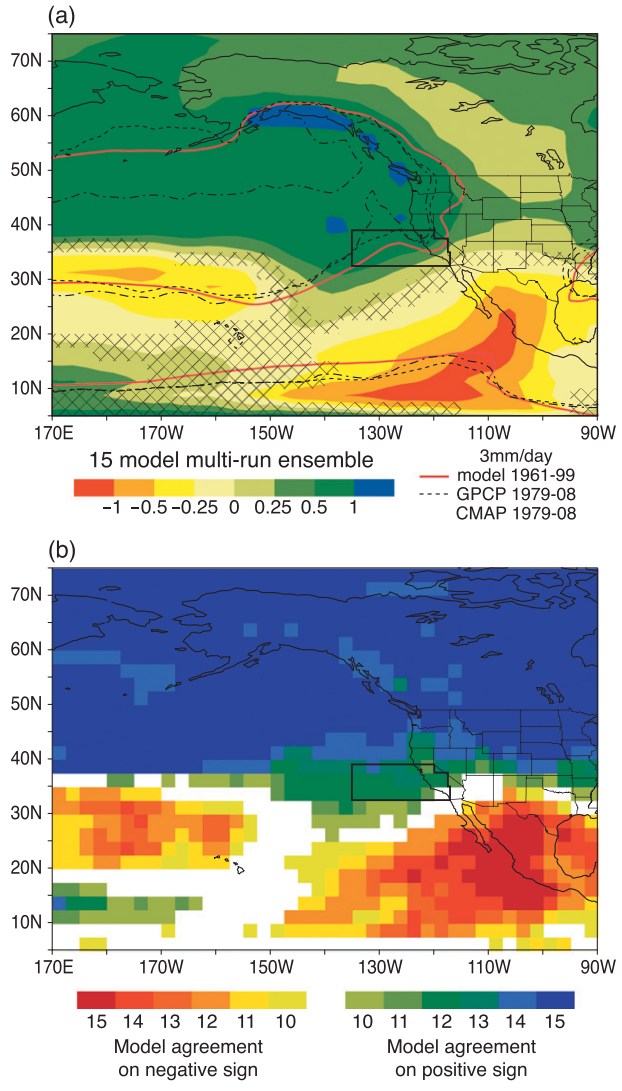

FIG. 1. DJF precipitation change measures in CMIP5 models for the end of the century (2070–99 average) relative to a base period of 1961–90 under the RCP8.5 forcing scenario. (a) Multimodel ensemble mean (15 models) precipitation change (mm day^{-1}). Red line shows the 3 mm day^{-1} contour from the MME mean base period climatology; dashed and dot-dashed lines show the same contour from the GPCP and CMAP datasets (1979–2008), respectively. Regions that do not pass a significance test for the MME mean relative to internal variability at the 95% level (see text) are cross-hatched. (b) Agreement on the sign of precipitation change among the model ensemble. Blue and green colors indicate a higher number of models (out of 15) agreeing on positive precipitation change; red colors indicate agreement on a negative precipitation change. Grid points with ≥10 models agreeing on sign pass a binomial test at the 94% level (see text); grid points not passing at this level are left blank. The box indicates the region used for averaging in later figures.

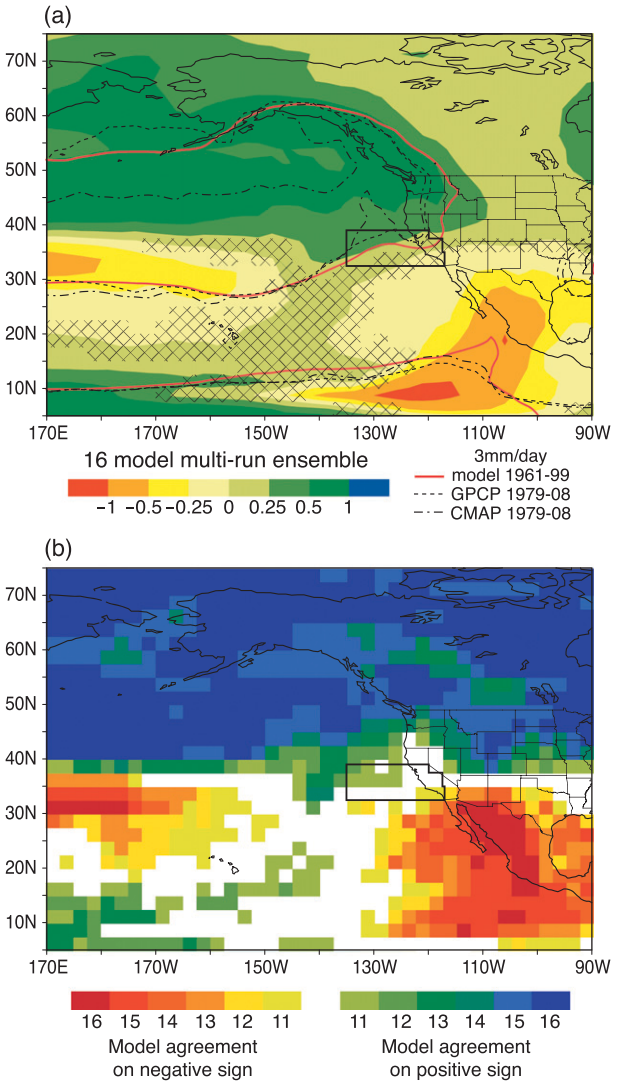

FIG. 2. As in Fig. 1, but for the CMIP3 ensemble under the SRES A2 forcing scenario and the MME mean (16 models) and agreement on the sign of precipitation (out of 15 models). Grid points with ≥11 models agreeing on sign pass a binomial test at the 96% level (see text).

a long thin band of reduced precipitation over the central North Pacific at the boundary between the subtropics and the midlatitudes (roughly 25°–35°N). Referring to the 3 mm day^{-1} contour of the MME mean climatology, one can see that the latter corresponds to a poleward shift in the precipitation associated with the storm track. In examining features in the MME precipitation change, we emphasize that the two-sided t test (95% level) used for shading in Figs. 1a and 2a tests only for sampling error in the MME mean relative to model internal variability—a necessary initial criterion—but does not test the thornier problem of intermodel agreement, as may be seen from substantial variations in spatial pattern (Fig. A1) exhibited by individual models. The problem of intermodel agreement is addressed first by agreement on sign (Figs. 1b and 2b) and then via area averages for

individual models below. The agreement on the sign of the precipitation change (Fig. 1b) echoes the large-scale features discussed above, with over 90% of the models agreeing on the precipitation increase north of approximately 40°N, and over 80% agreeing on the drying trend over much of the subtropical regions just described including 90% agreement in northern Mexico. Grid points for which 10 of 15 models agree on sign pass a binomial test to reject the null hypothesis of equal probability of positive or negative sign at the 94% level. The region with over 10 models (two-thirds of the ensemble) agreeing on sign also roughly corresponds to the region for which the MME mean passes the *t* test at the 95% level relative to internal variability. Further discussion of significance tests in Fig. 1 and combined sign and *t*-test criteria is provided in the appendix (Fig. A2).

The large-scale changes with subtropical precipitation reductions and midlatitude increases are commonly discussed in terms of the ''rich-get-richer'' mechanism (Chou and Neelin 2004; Held and Soden 2006; Trenberth et al. 2007; Trenberth 2011; Durack et al. 2012) in which moisture increases associated with warmer temperatures tend to yield precipitation increases in regions of moisture convergence and decreases in regions of moisture divergence in the historical-period climatology, even if there is no major change in the statistics of the flow field. While this mechanism tends to set the stage at large scales, dynamical feedbacks, with changes in the circulation affecting precipitation changes, can be important at regional scales (Chou and Neelin 2004; Chou et al. 2009; Seager et al. 2010; Hsu and Li 2012).

Turning from the large-scale features to the regional aspects relevant to the California coast, the CMIP5 MME mean (Fig. 1a) exhibits an increase in precipitation over the oceanic regions immediately to the west. This increase occurs where the southward boundary of the climatological storm track (see the 3 mm day^{-1} contour in Fig. 1a) angles northeastward onto the coast. The increase in precipitation in this region contrasts with the decrease that occurs at these latitudes over most of the western and central Pacific. Because this feature is potentially important to California water resource planning but occurs at regional scale for a region that in prior assessments had high uncertainty, the remainder of this paper will aim to flesh out the factors that might assist in assessing to what degree it can be trusted. We will refer to this region as the storm-track extension or jet extension region since it will be shown to be associated with an eastward extension toward the coast of both the climatological storm-track precipitation region and the region of strong Pacific jet stream that steers the storms, as elaborated below.

The intermodel agreement on the sign of the precipitation change decreases southward over this region in the CMIP5 models (Fig. 1b). At the latitudes of Oregon and most of northern California, almost all CMIP5 models agree on an increase over the coastal and neighboring ocean region; at the latitudes corresponding to central California, 13 of 15 agree on an increase, but by 30°N, less than two-thirds of the models show an increase. In terms of California water resources, the rainfall associated with storms arriving on the Sierras is a key feature, so high agreement on winter season rainfall at these latitudes would be positive news not only for central California but also for Southern California, because of the existing infrastructure for water transfer, despite less clear agreement on rainfall change from Los Angeles southward. Comparing to the CMIP3 ensemble (Fig. 2), in both the MME mean and agreement on sign, the shift of the positive region is notable—but precisely because it is a shift of a boundary, it must be evaluated critically. We note that hints of the storm-track extension feature off the California coast may be seen in the CMIP3 models, but they are not nearly as developed as in the CMIP5 models. While this feature represents a departure from zonal symmetry, we can begin by examining the precipitation simulation of the individual CMIP5 models as a function of latitude for an average over this feature.

Figure 3a provides a sense of the latitude dependence of the simulated rainfall in the historical period in the CMIP5 models compared to observations and for the end of century over the range of latitudes approximately corresponding to the California coast. Because we do not expect models of these resolutions to do a good job of topographic rainfall within the state, this figure examines a longitude average indicative of the storm-track precipitation arriving at the coast, using the longitude range of the box shown in Fig. 1 (i.e., from 135°W to the California onshore grid box shown in the figure); between 39° and 42°N the longitude range is the same as at 39°N. In the historical period, the multimodel ensemble mean qualitatively tracks the latitude dependence of the satellite estimates of the observed. At 32°N in Southern California, the amplitude of the MME mean is higher than GPCP and CMAP by about 27% and 36%, respectively. At 42°N, the latitude of the California–Oregon border, the MME mean is slightly lower than GPCP, while CMAP gives an estimate 50% lower than GPCP.

Figure 3b shows the same latitude slice for the model precipitation at the end of the century. The poleward precipitation gradient tends to increase as well as the amplitude of the rainfall in most models. The difference between end-of-century and the base (Fig. 3c) shows positive precipitation increasing with latitude in most

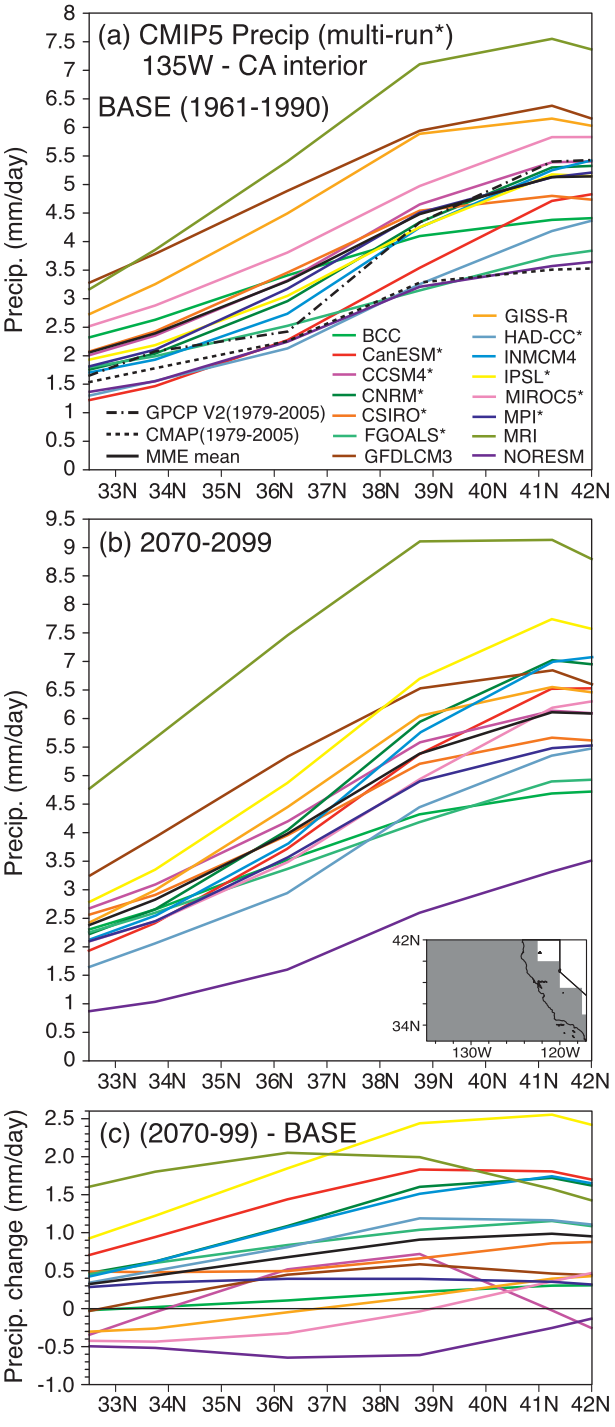

FIG. 3. Latitude cross section of precipitation (mm day^{-1}) averaged over the longitude band where the storm tracks arrive at the California coast [135°W to the California land region shaded in the inset in (b)]. (a) Model precipitation for the historical base period (1961–90), with CMAP and GPCP observational estimates (dashed and dash-dotted, respectively; 1979–2005). (b) End-of-century (2070–99) model precipitation. (c) Model end-of-century precipitation change relative to base period; MME mean shown as black curve and individual models given by colored curves (see the Table A1 for model acronyms in legend).

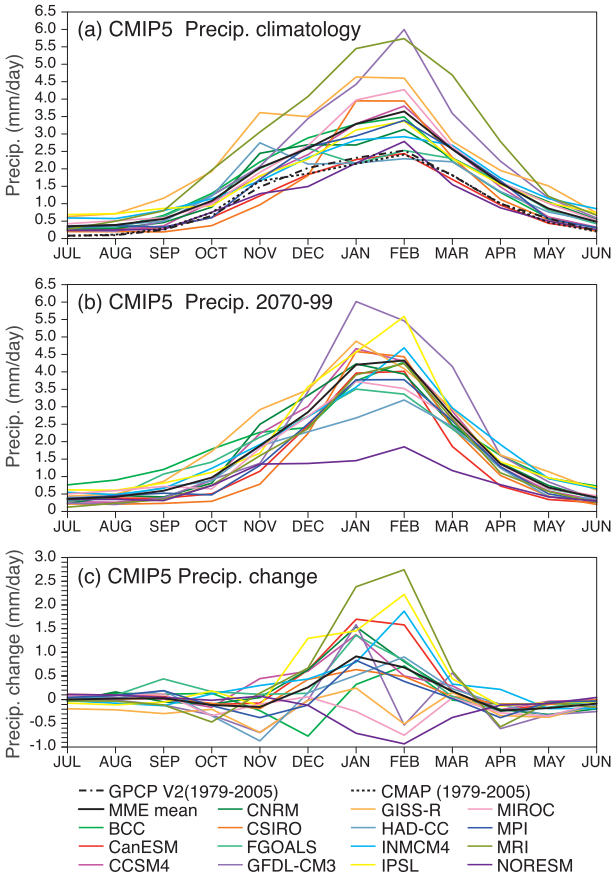

FIG. 4. Seasonal cycle of precipitation (mm day^{-1}) for the averaging region shown in Fig. 1. MME mean shown as black curve and individual models given by colored curves (acronyms in legend). (a) Model precipitation for the historical base period (1961–90), with CMAP and GPCP observational estimates (dashed and dash-dotted, respectively; 1979–2005). (b) End-of-century (2070–99) model precipitation. (c) Model end-of-century precipitation change relative to base period.

models. One model has a decrease throughout the range; in a few models, the gradient of the change yields a decrease the southern part of the range.

Another aspect to be taken into account is potential change in the seasonal cycle. The agreement shown here is for the main winter months, December–February. However significant contributions to California annual rainfall also come from October–November and March (Cayan and Roads 1984). Figure 4 shows the seasonal cycle of the precipitation changes in an area average over the region shown in Fig. 1. A substantial plurality of models exhibits a decrease in November, with the MME mean near zero, standing as a caveat on uncertainty in the potential seasonal distribution of precipitation, especially during the onset season. It serves to underline the winter season precipitation considered here as the season of higher agreement, which is potentially highly

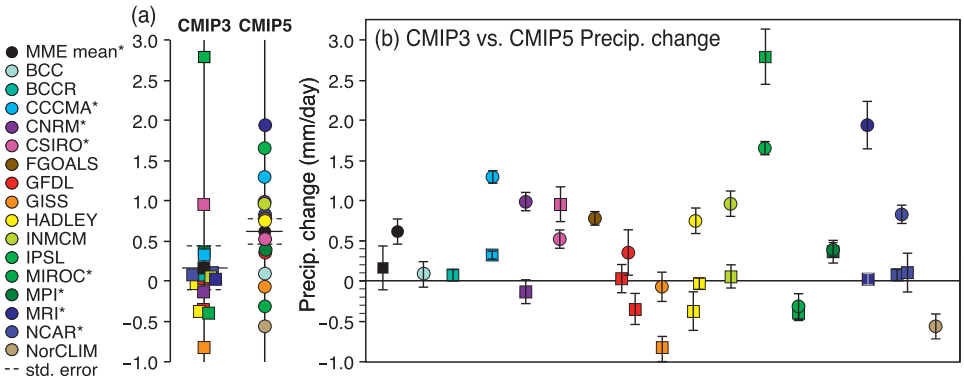

FIG. 5. DJF precipitation changes for an area average over the ocean just off the coast of California and extending into the California coastline (area shown in Fig. 1) for CMIP3 models (squares) and CMIP5 models (circles). (a) Values for all models with the MME mean for CMIP3 and CMIP5 respectively. (b) The MME mean for each of CMIP3 and CMIP5 shown at the left with error bars corresponding to ±1 standard error among the ensemble values (0.20 and 0.17 mm day^{-1}, respectively). Values from individual models are shown with model versions from the same modeling group shown in the same place on the abscissa. Error bars denote ±1 standard error estimates due to natural variability from a given model (all runs). Asterisks in the legend denote models with multiple runs included in the average. There are two CMIP3 entries for GFDL and for two variants of the NCAR model (see appendix for details).

useful because it corresponds to the season of high contribution to snowpack buildup.

3. The storm-track extension region and relationship to subtropical jet extension

a. Regional-scale changes

Figure 5 shows end-of-century DJF precipitation changes in an area average over the region shown in Fig. 1 where the storm track reaches the California coast from 32° to 39°N. The latitude band includes the southern and central California coast, and latitudes corresponding to the Sacramento–San Joaquin delta in Northern California. The southern portion of the domain down to the latitude of the Mexican border is included so as not to fine-tune the latitude range to those that exhibit the strongest increases. The northernmost portion of California is excluded because these regions are further removed from Southern California water resource impacts, and projections of precipitation increases appear clearer as one moves north. In other words, the latitude range of the box aims to assess the region that was of uncertain sign in the CMIP3 models. The oceanic westward extent corresponds to that of the storm-track extension region discussed following Fig. 1, which will be investigated in this section to determine its relationship to an extension of the region of the Pacific with a strong subtropical jet. This region also corresponds to a region that tends to differ between CMIP3 and CMIP5.

Both CMIP3 and CMIP5 have roughly comparable scatter among the models for the projected precipitation change in this region (standard deviations of 1.11 and 0.80 for 16 and 15 models, respectively, yield standard errors of the MME mean of 0.20 for CMIP3 and 0.17 for CMIP5), although the distributions differ in that CMIP3 has two noticeable outliers (Fig. 5a). The MME mean for the CMIP5 models is shifted distinctly above zero (differs from zero at better than the 99% confidence level, with a p value of 0.0035, by a two-sided t test), whereas the MME mean for CMIP3 was not well distinguished from zero (less than 60% confidence level). If one were to assume the CMIP3 ensemble to be independent of the CMIP5 ensemble, the MME means differ at the 90% confidence interval, a p value of 0.104, by a two-sided t test for the difference of independent means. However, 12 of the models have both a CMIP3 and a CMIP5 version, and two of these have two CMIP3 counterparts (the GFDL and NCAR models; see discussion of Table A1). A set of t tests for the difference of dependent means among the models that have counterparts in both intercomparisons was carried out for each of the four combinations that result from choosing one of the GFDL and one of the NCAR CMIP3 versions. For each case, the difference is taken between CMIP3 and CMIP5 values for each model and the hypothesis that the mean of these is zero is tested. The four cases yield differences significant at the 93%–95% level. Figure 5b shows that the CMIP5 version has systematically more rainfall for eight models and CMIP3 for two (with two models having small change). The precipitation change associated with storm tracks coming onto California in the CMIP5 models is thus both different from the previous intercomparison and clearly

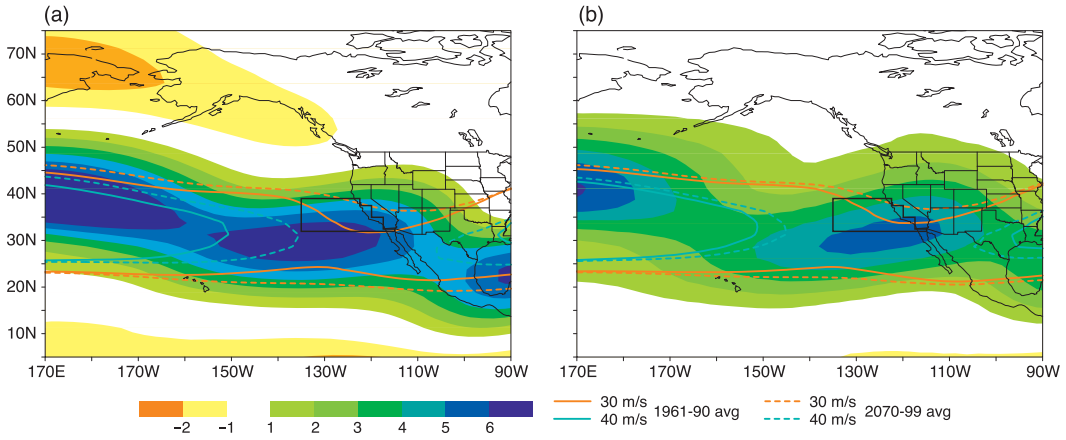

FIG. 6. DJF 200-mbar zonal wind change (shading) for the end of century (2070–99 average) relative to a base period of 1961–90 for the multimodel ensemble mean for (a) CMIP5 and (b) CMIP3. The 30 and 40 m s^{-1} contours of the 200-mbar zonal wind are shown for the base period (solid contours) and the end-of-century (dashed contours), respectively.

positive in this regional average. Changes in the averaging region that shift the box slightly northward, or exclude part of the Southern California coastal region that shows smaller MME mean changes in Fig. 1 tend to increase these differences.

We now turn to the question of whether this is associated with an identifiable physical pathway, in particular the hypothesized relationship to a change in the jet stream. Figure 6 shows the MME mean upper-level zonal winds, using the 30 and 40 m s^{-1} contours to indicate the region of strong jet stream. For the CMIP5 models (Fig. 6a), the region exceeding 30 m s^{-1} extends across the Pacific for the historical period at a latitude of roughly 25°–45°N. In the end-of-century simulation, this broadens, corresponding to a strengthening of the jet, especially in the region just off the coast of North America. The region where the jet exceeds 40 m s^{-1}, from the western Pacific to near 150°W in the base period, extends about 15° farther eastward at the end of century. The change in speed relative to the historical period shows the jet increasing in zonal velocity by over 6 m s^{-1} over most longitudes, but in the central Pacific this increase occurs at the northern flank of the jet, while in the eastern Pacific the increase extends the jet at the latitude of its core. This region in the eastern Pacific corresponds to the angled region of the southern flank of the storm track described following Fig. 1, where storms tend to veer northward. The increased jet stream zonal velocity at the steering level is associated with a tendency to direct storms toward the coast of California in models and observations of natural variability (Held et al. 1989; Chen and Van den Dool 1997; Straus and Shukla 1997). (Figure A3 provides an overview of this response for individual models, and the pattern of jet extension in this eastern Pacific region occurs in almost every case.) The main exception is the NorESM model, which actually exhibits a decrease in jet velocity in this region (and correspondingly has a decrease in precipitation). Another outlier in wind pattern, the BCC model, does exhibit an increase in the jet speed but it occurs on the south flank of the climatological jet in the eastern Pacific. For reference in discussion below, Fig. 6b shows the corresponding behavior for the CMIP3 MME mean. While there is an increase in jet speed with global warming that is qualitatively similar to that seen for CMIP5 in Fig. 6a, the eastern Pacific response is weaker and positioned in a way that is less effective at extending the strongest part of the jet. For instance, the increase in the eastward extent of the 40 m s^{-1} contour relative to the base period is much smaller in CMIP3 than in CMIP5.

To check whether a relationship between zonal wind changes associated with the jet extension and precipitation holds for the CMIP5 models under global warming, Fig. 7 shows the change in precipitation for the area average discussed in Fig. 5 as a function of the zonal wind change averaged over the same storm-track extension region in the eastern Pacific and the California coast for CMIP5 (Fig. 7a) and CMIP3 (Fig. 7b). Three-dimensional zonal wind fields are available for only a subset of runs so a single run is used for each model to ensure consistency of the precipitation–wind relationship. In CMIP5 (Fig. 7a), most models exhibit a positive increase in both quantities, and the few with small or negative wind changes have small or negative precipitation changes. The correlation coefficient between the two indices, calculated for the regression line shown for the points on this plot, is 0.76. The main outlier in Fig. 7a that has a substantial change in jet speed but not in

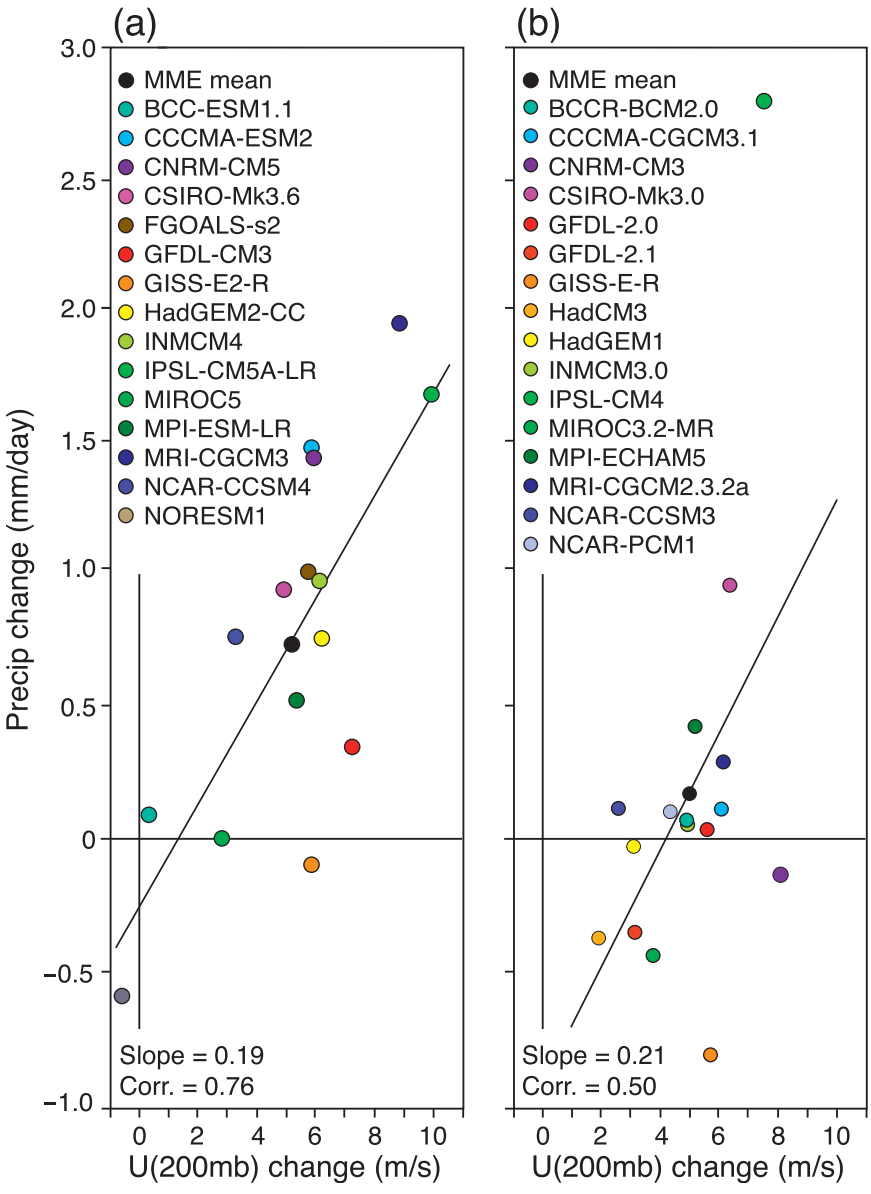

FIG. 7. DJF precipitation averaged over the region in Fig. 1 vs DJF 200-mbar zonal wind averaged over the same region, for (a) CMIP5 and (b) CMIP3 models. The correlation coefficients (0.76 and 0.50) and slopes [0.19 and 0.21 mm day^{-1} (m s^{-1})$^{-1}$, respectively] are associated with the linear regression line shown.

precipitation is the GISS model. GISS has the strongest climatological zonal jet in this region, so it is possible that the increase in zonal wind in this case has little additional effect in carrying precipitating systems to this portion of the coast.

In CMIP3 models (Fig. 7b), the correlation in the relationship to the zonal wind index is lower (0.50), although the regression slope is similar, suggesting that while some relationship to jet changes might be present, it is only a secondary contributing mechanism to the precipitation change in this area average in CMIP3. This appears consistent with the differences in the spatial pattern of the jet stream increases seen in Fig. 6, with the eastern Pacific intensification of the jet stream in CMIP5 better positioned to extend the core of the jet eastward in a location likely to be impactful in steering storms.

This potential contribution of the jet extension in CMIP5 should be placed in context of other possible mechanisms. First, the basic rich-get-richer mechanism due to increases in moisture that yields precipitation reductions in the subtropical moisture-divergence regions and precipitation increases at midlatitudes, as outlined in

section 2, will certainly have variations from model to model. This is the default hypothesis for intermodel scatter in precipitation change over California in CMIP3. However, the strong similarity between CMIP3 and CMIP5 MME mean precipitation change in Figs. 1 and 2 in the main features of surrounding regions—the reduction region over Mexico and the eastern Pacific between 10° and 25°N, the reduction in the central Pacific near 30°N, and the increases poleward of California—makes this less satisfying as an explanation of the differences in the storm-track extension region. Second, one might consider whether increases in resolution between CMIP3 and CMIP5 might impact California precipitation. While a majority of the CMIP5 models have at least a slight increase in resolution, and this could well affect simulated jet stream or precipitation changes in particular models, there does not appear to be a clear relationship between resolution (Table A1) and the area-average precipitation change in Fig. 5. Third, we cannot exclude the possibility that the sum of various revisions of model parameterizations might contribute to the difference in CMIP5 in this region, although we have not been able to discern signatures of such changes in climatology or on the precipitation change in surrounding regions. In sum, we argue that the jet-extension changes constitute a factor that should be taken into account in examination of these precipitation changes.

Locally, the relationship between zonal wind anomalies of the jet extension and the increase of precipitation arriving at the California coast is analogous to the jet and storm-track changes related to El Niño (Held et al. 1989; Chen and Van den Dool 1997; Straus and Shukla 1997) that affect California rainfall in interannual variability (Redmond and Koch 1991; Dettinger et al. 1998; Cayan et al. 1999; Leung et al. 2003). However, the causes of the jet extension itself are not simply related to equatorial Pacific SST changes: correlation of the area average zonal wind and precipitation to the Niño-3.4 index in the equatorial Pacific is less than 0.3 and about 0.1, respectively. The lack of relationship between subtropical jet changes and equatorial Pacific SST is consistent with Lu et al. (2008), who contrasted jet changes under global warming with those under El Niño. Given the large zonal scale of the jet changes in Fig. 7 (and Fig. A3), it is likely that the jet changes arise from the global-scale mechanisms discussed below, and it is simply the regional precipitation impacts that follow a local physical pathway akin to the jet-related effects active during El Niño.

b. *Storm-track extension relationships in interannual variability and to California land regions*

In previous sections we have focused on a regional-scale average that included a substantial area off the coast because of caution about trusting precipitation simulations over California land regions where the arrival of storms over land and interaction with topography add complex small-scale effects. Bearing these caveats in mind, in this subsection we provide some basic indicators of the relationship of the storm-track extension box average used above to a smaller-scale box average more typical of California land regions, and of the modeled and observed relationships between 200-mbar wind in the jet extension region to this index of California precipitation. This is undertaken for the CMIP5 models, for which the jet extension argument seems to be most relevant.

Figure 8 shows relationships between precipitation averaged over the storm-track extension box to precipitation averaged over a subset of this region that approximates California within the latitude band from 32.5° to 39°N based on the 2.5° grid (and omitting desert regions east of San Diego). Figure 8a shows this for simulated precipitation change at the end of century relative to the 1961–90 base period for the CMIP5 models. Most models simulate changes over the California averaging regions that are closely tied to the changes simulated over the larger storm-track region, with the slope implying that the California box typically exhibits slightly smaller precipitation change per unit change in the larger box average. Two models (NCAR and NorClim) deviate from this relationship, with changes exceeding 0.5 mm day^{-1} of different sign in the California region than in the larger region average. The overall correlation between the two averaging areas for the ensemble is 0.7.

Although interannual variability is not necessarily a good prototype for global warming changes, the relationships described in the previous subsection suggest that examining the model behavior in the historical period and comparing to observations of interannual variability can serve as useful background. Figures 8b–p show how variation in wintertime (DJF) precipitation in the larger averaging region relates to that in the California averaging region as simulated in the models. In choosing the evaluation period (1961–2000) displayed, a compromise was made between using an interval closer to the satellite record interval, but not using years beyond 2000 because comparison was also made to CMIP3, in which the switchover from the historical period to forcing scenarios from 2001 can have a nontrivial disjuncture. The models exhibit high correlation, typically exceeding 0.9, between DJF precipitation in the larger and smaller averaging regions for interannual variability (single runs have been used for each model to provide an analog to observed time series). This correlation exceeding 0.9 also holds in the GPCP v2.2 observational

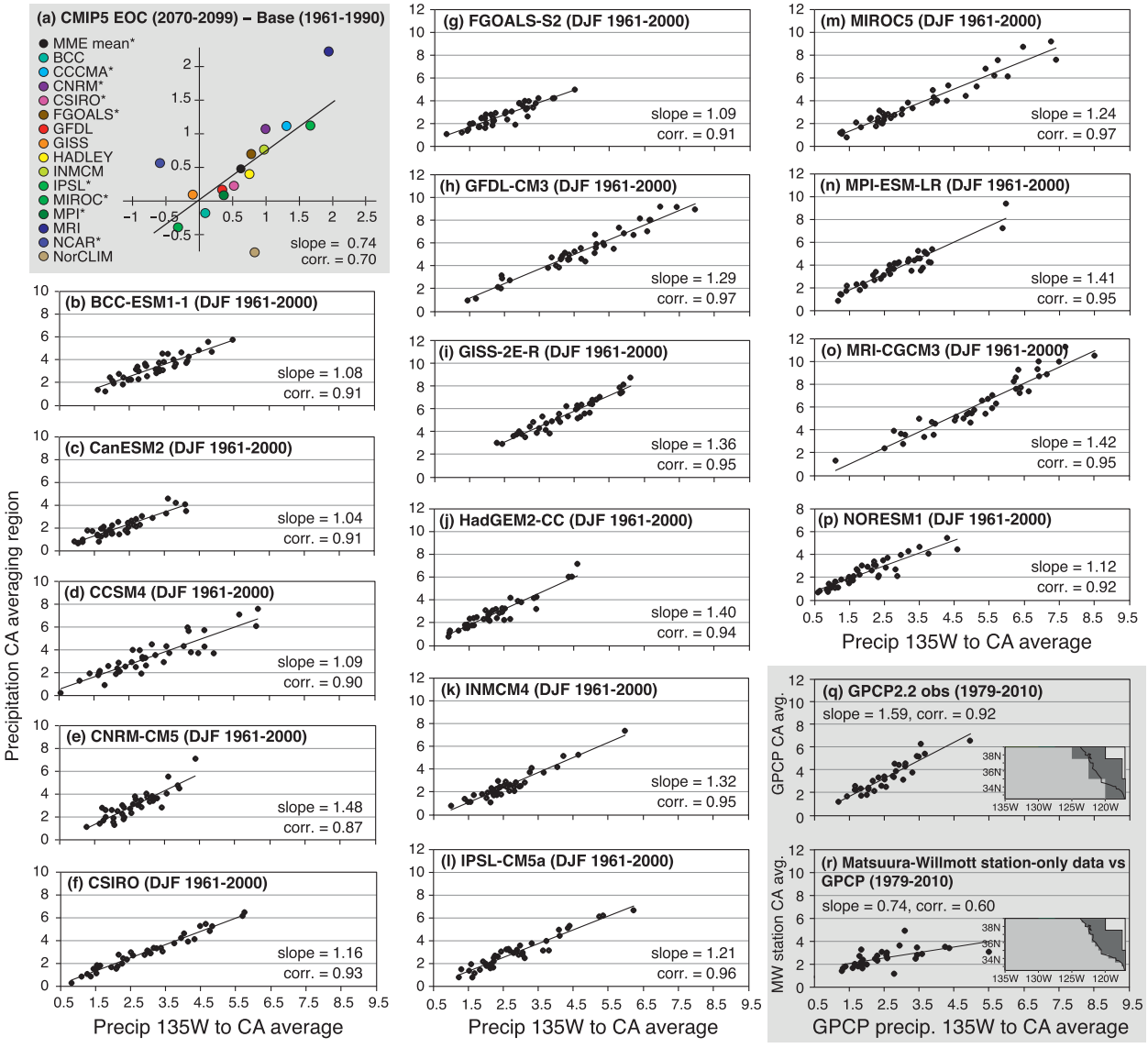

FIG. 8. Relationships between DJF precipitation (mm day^{-1}) averaged over the storm-track extension box (32.5°–39°N, 135°W to California interior) on the x axis to DJF precipitation (mm day^{-1}) averaged over a subset of this region approximating California coastal and interior regions on the y axis. (a) Relationships for end-of-century precipitation change between the larger and smaller averaging regions for the CMIP5 models. (b)–(p) Relationships between precipitation in the larger and smaller averaging regions for year-to year variability in DJF precipitation simulated in each of the models (1961–2000). (q) As in (b)–(p), but for GPCP v2.2 observational estimate (merged station and remote sensing product) for 1979–2010. Inset shows averaging regions applied to GPCP and all model simulations. The larger averaging region includes both light and dark gray shading; the dark gray denotes the subset used in the smaller averaging region. (r) Matsuura–Willmott interpolated land station-only observational estimate for a similar California averaging area (y axis) vs GPCP for the larger averaging area for 1979–2010. Inset dark gray shading shows the averaging area for the station-only data (the larger averaging area is the same as in other panels).

estimate (which includes land station data merged with remote sensing retrievals) for the same averaging regions (Fig. 8q). The correlation of the large-box GPCP precipitation to a California-box land station–only observational estimate from the University of Delaware (Matsuura and Willmott 2012 dataset) is somewhat lower. This could potentially be due to the station-only data having only point sampling, which tends to yield higher variance, although Caldwell (2010) finds the station-only dataset to have higher mean California winter precipitation. Note also that for the station-only data, available at 0.5° resolution but only for land points, the averaging area here differs slightly at coastal points from the California averaging area defined on the 2.5°

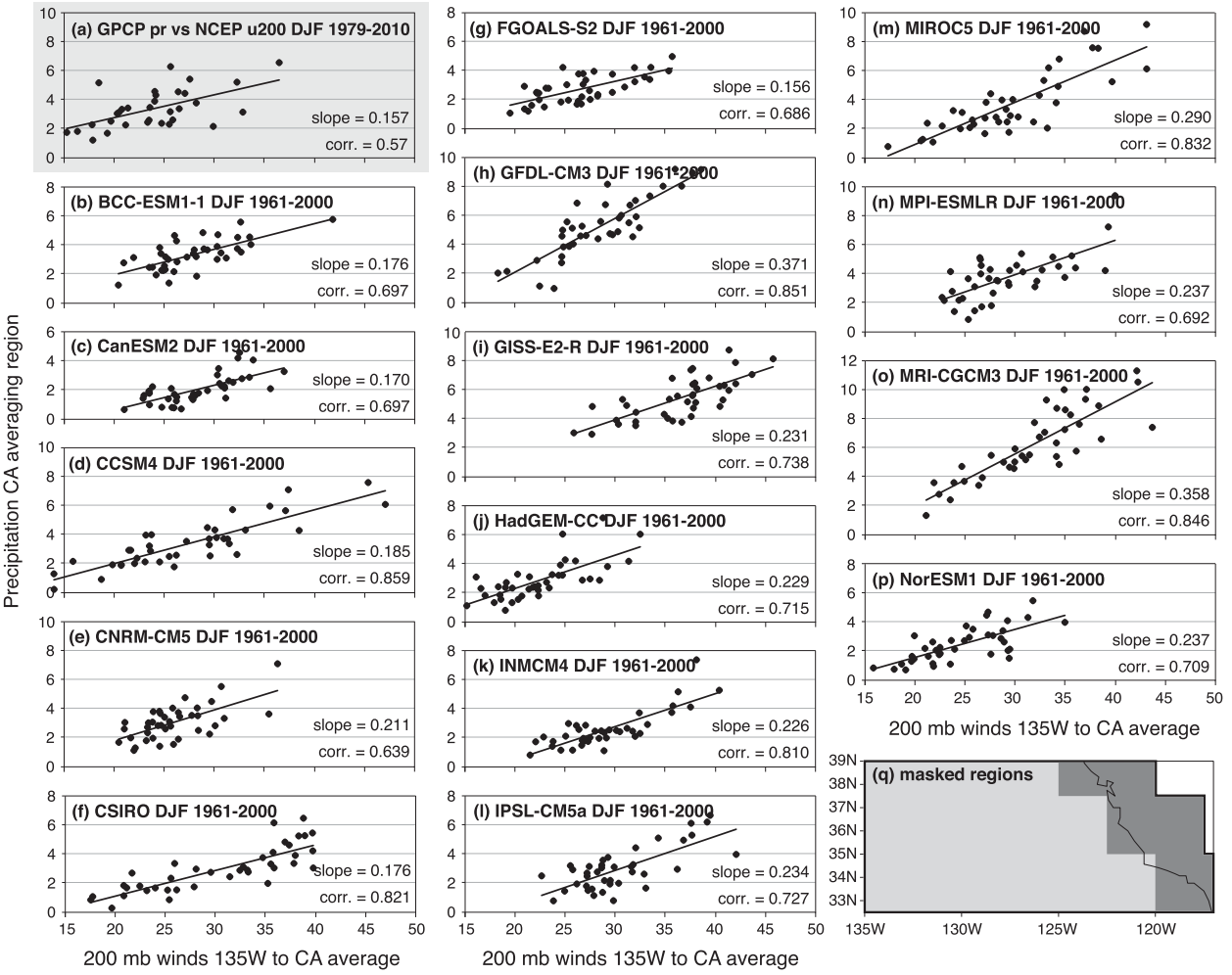

FIG. 9. Relationships between DJF 200-mbar zonal wind averaged over the storm-track extension box (135°W to California interior, 32.5°–39°N) on the *x* axis to DJF precipitation averaged over a subset of this region approximating California coastal and interior regions on the *y* axis. (a) Relationships for the NCEP reanalysis winds and GPCP v2.2 observational precipitation estimate for DJF year-to-year variability (1979–2010). (b)–(p) As in (a), but for each of the CMIP5 model simulations (1961–2000). (q) Averaging regions repeated for reference from Fig. 8q. The larger averaging region used for the wind includes both light and dark gray shading; the dark gray denotes the smaller averaging region used for precipitation.

grid (Figs. 8q,r, inset). The slope of this relation differs in the two observational estimates (1.6 and 0.74, respectively), with the GPCP suggesting that the California averaging region is slightly larger and the station-only dataset suggesting the California averaging region precipitation slightly smaller than the precipitation averaged over the larger region. For the models the slope ranges from approximately 1 up to 1.5, within the observational range.

Overall, in the observations and in all models the basic relationship between the California averaging region and the larger storm-track region holds well in interannual variability, with the California box having precipitation anomalies not too much higher or lower than the corresponding anomaly in the larger box average. This behavior is concordant with the behavior of all the CMIP5 models except for two in the global warming changes. This appears consistent with viewing the changes in the storm track coming onto the coast as a likely substantial factor in setting the changes in California precipitation, although obviously it should not be taken as the sole factor.

We can further ask if any constraint on the relationship between steering-level wind and California precipitation can be obtained from interannual variability. Figure 9 shows the relationship of DJF precipitation averaged over the California averaging region to the DJF 200-mbar zonal wind averaged over the jet

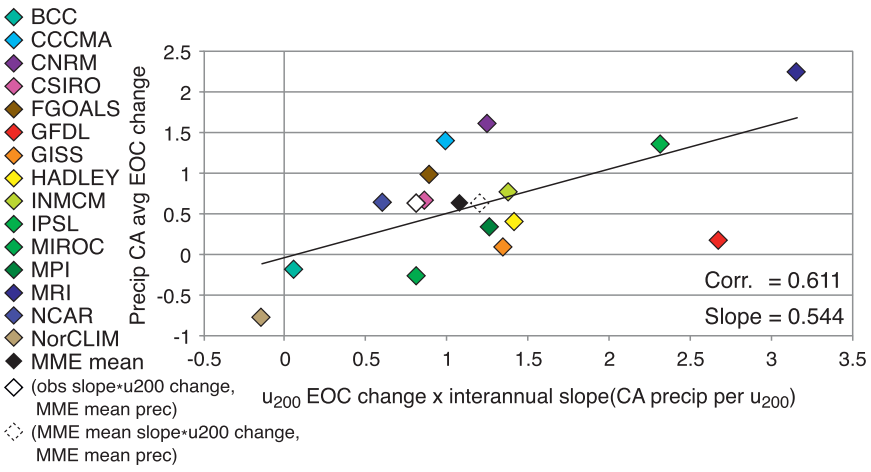

FIG. 10. CMIP5 model end-of-century DJF precipitation change (2070–99 minus 1961–90) on the *y* axis as a function of a precipitation measure constructed from each model's end-of-century zonal wind change (averaged 135°W to California) times the slope from Fig. 9 for the California averaging region precipitation change per unit change in zonal wind. Also shown are points for the multimodel ensemble mean (black) and a variant where the multimodel ensemble mean slope is multiplied by the multimodel ensemble mean wind change (dashed diamond). The solid white diamond gives the corresponding point when the observed slope (from Fig. 9a) times the multimodel ensemble mean wind is used.

extension region, u_{200} (averaging regions are repeated in Fig. 9q for reference) for the CMIP5 models and observations. The time periods are chosen as in Fig. 8. Each of the models exhibits a reasonably strong relationship with correlations ranging from 0.64 to 0.86 over the 4 decade period, and slopes ranging from 0.16 to 0.37 mm day^{-1} (m s^{-1})$^{-1}$. The relationship between the GPCP observational precipitation product and NCEP reanalysis winds, over a 3 decade period, exhibits a roughly similar relation, with a correlation about 0.6 and a slope of 0.16 mm day^{-1} (m s^{-1})$^{-1}$ corresponding to the lower end of the model range.

Does this slope in interannual variability bear any relationship to model precipitation increases in the global warming case? Figure 10 provides one way of checking this. The end-of-century precipitation change (2070–99 minus 1960–90) for each model (averaged over all available runs) is shown as a function of a precipitation measure constructed from the slopes in Fig. 9. Specifically, the slope obtained from interannual variability for each model (California precipitation change per unit change in u_{200}) is multiplied by that model's end-of-century change in u_{200} over the averaging region.

With a correlation of 0.61, this quantity is far from a perfect predictor of end-of-century precipitation change, but the relationship appears sufficient to warrant placing a value associated with the observational estimate of the slope on the plot. This is done by taking the slope in Fig. 9a from observational estimates of interannual variability and multiplying by the MME mean value of u_{200} end-of-century change (white diamond; plotted with the MME mean *y*-axis value). This may be compared to the point with the *x*-axis value obtained from the average of the model slopes in Fig. 9 multiplied by the MME mean value of u_{200} change (dashed diamond). The closeness of the latter to the MME mean (black diamond) suggests that no substantial bias is incurred by using the multimodel ensemble mean u_{200}. The point using the observed slope (white diamond) has slightly lower reconstructed precipitation than the MME mean, but the bulk of the models are not too far removed from it, adding modest circumstantial evidence that the models are performing reasonably in this respect. Dropping the highest and lowest models based on the *x*-axis value results in pruning the highest and lowest values of the predicted end-of-century precipitation change, although substantial scatter would remain due to factors not controlled for by this analysis. Overall, the results in this subsection suggest that the positive contribution to California precipitation associated with the jet extension tends to carry down to the smaller averaging region and that the model physics simulating the California precipitation response to jet changes is roughly consistent with observations, albeit with higher amplitude in some models.

4. Discussion

While in many regions the results of the CMIP5 model ensemble are highly consistent with results previously

documented for CMIP3, here we examine one region of difference that may have potentially important implications for California water resources. By several measures the precipitation increase in the regional-scale feature of the storm track–related DJF precipitation arriving at the coast indicates significant increases in the CMIP5 ensemble, and this ensemble behavior is significantly different from that of the CMIP3 ensemble. Because California lies near the boundary between robust precipitation increases to the north and decreases in the subtropics, we underline the need for caution in assessments of projected precipitation change, especially as evaluated from global models. We thus highlight a hypothesized physical pathway involving a contribution to precipitation change in the region coming onto the California coast associated with changes in the upper tropospheric subtropical jet in this region (other large-scale mechanisms, including those that establish the north–south gradient, may also play a role in intermodel differences). This pathway should influence results in regional climate models and could thus be further evaluated in these.

These relationships are assessed in a storm-track extension averaging region that includes coastal ocean regions as well as California land regions for which the MME mean precipitation increase in CMIP5 is significantly different from zero at the 99% and significantly different from CMIP3 at the 90%–95% level, depending on the test. This region correlates with California land-region averages in both projected precipitation changes and interannual variability, but with reduced certainty at smaller scales and over land regions. There is a substantial northward gradient in this precipitation change, so while increases discussed at these regional averages might be beneficial to the system of water redistribution that exists in the state, they should not be taken to imply precipitation increases everywhere in the state. In particular, Southern California regions from Los Angeles to San Diego, where local precipitation is a substantial contributor to groundwater resources, have uncertain sign in the CMIP5 ensemble. Impacts of changes in temperature on snowmelt are likely to affect water resources (Barnett et al. 2008; Cayan et al. 2008) but are not assessed here.

The increases in precipitation in the region coming onto the California coast in the CMIP5 ensemble have a substantial relationship to changes in the upper tropospheric subtropical jet in this region. Analogous jet–rainfall relationships in interannual variability are reasonably well simulated in the model ensemble. The changes in the jet under global warming appear to be essentially those that have been previously discussed for the changes in the large-scale zonal-mean jet, although regional-scale changes in the eastern Pacific may be particularly important. Although there can be in individual models (Fig. A3) some variation in the jet increase as a function of longitude over North America, the strengthening of zonal-mean upper-level jet seen in the MME mean (Fig. 6) seems consistent with changes previously examined for the zonal mean (Yin 2005; Lorenz and DeWeaver 2007). While changes in subtropical jet are often referred to in terms of a poleward shift in latitude, they are better described as a strengthening of the jet at upper levels accompanied by an increase both upward and slightly poleward of the main jet axis (Lorenz and DeWeaver 2007; their Fig. 5) due to changes in the tropopause height, with some contributions from changes in baroclinic instability (Yin 2005; Frierson et al. 2007).

Although the change in subtropical jet zonal wind appears to arise at very large scales, the California rainfall changes provide an example of how this large-scale change can interact with a regional feature of the climatology to produce effects locally that would not easily be anticipated from zonal average considerations. The increases in zonal wind speed, here occurring in the regions where the climatological storm tracks angle poleward, are associated with steering storms more directly to the California coast by the same process as occurs in natural variability (Held et al. 1989; Chen and Van den Dool 1997; Straus and Shukla 1997). In discussing precipitation changes under global warming, there is a tendency to use rules of thumb associated with zonal-average or large-scale considerations because the larger scales tend to have smaller uncertainty than regional scales. The results in the CMIP5 models for California precipitation provide an example where this would oversimplify. While precipitation associated with the storm track is shifted poleward in the western and central Pacific, the physical pathway associated with jet extension results instead in what is better described as an eastward shift in the portion of the storm track that angles northward toward northern California in the climatology. Diagnostics based on this pathway are hypothesized to be useful in informing downscaling approaches, mechanism studies, and detection and attribution studies seeking further assessment of the positive winter precipitation change seen in the CMIP5 models in storm-track precipitation arriving at much of the coast of California.

Acknowledgments. This work was supported in part by the NOAA Climate Program Office Modeling, Analysis, Predictions and Projections (MAPP) Program under Grant NA11OAR4310099 as part of the CMIP5 Task Force and National Science Foundation Grant AGS-1102838. We acknowledge the World Climate

TABLE A1. Modeling groups and model versions for CMIP3 and CMIP5.

Modeling center or group, institute acronym, country	CMIP3 model name (number of model runs)	CMIP5 model name (number of model runs)
Beijing Climate Center (BCC), China Meteorological Administration, China		BCC Climate System Model, version 1.1. (BCC-CSM1.1) (1) 2.8125° × 2.8125°
Bjerknes Centre for Climate Research (BCCR), Norway	BCCR Bergen Climate Model, version 2.0 (BCCR-BCM2.0) (1) 2.8125° × 2.8125°	
Canadian Centre for Climate Modeling and Analysis (CCCma), Canada	CCCma Coupled Global Climate Model, version 3.1 (CGCM3.1) (5) 3.75° × 3.75°	Second Generation Canadian Earth System Model (CanESM2) (5) 2.8125° × 2.8125°
Centre National de Recherches Meteorologiques (CNRM)/ Centre Europeen de Recherche et Formation Avancées en Calcul Scientifique (CERFACS), France	CNRM Coupled Global Climate Model, version 3 (CNRM-CM3) (1) 2.8125° × 2.8125°	CNRM Coupled Global Climate Model, version 5 (CNRM-CM5.1) (5) 1.40625° × 1.40625°
Commonwealth Scientific and Industrial Research Organization (CSIRO)/Queensland Climate Change Centre of Excellence (QCCCE), Australia	CSIRO Mark, version 3.0 (CSIRO Mk 3.0) (1) 1.875° × 1.875°	CSIRO Mark, version 3.6 (CSIRO Mk 3.6) (5) 1.875° × 1.875°
State Key Laboratory of Numerical Modeling for Atmospheric Sciences and Geophysical Fluid Dynamics (LASG), Institute of Atmospheric Physics, Chinese Academy of Sciences, China		Flexible Global Ocean–Atmosphere–Land System Model gridpoint, second spectral version (FGOALS-S2.0) (3) 2.8125° × 1.65°
Geophysical Fluid Dynamics Laboratory (GFDL), United States	GFDL Climate Model, version 2.0 (GFDL-CM2.0) (1); GFDL Climate Model, version 2.1 (GFDL-CM2.1) (1) 2.5° × 2.0°	GFDL Climate Model, version 3 (GFDL-CM3) (1) 2.5° × 2.0°
National Aeronautics and Space Administration (NASA) Goddard Institute for Space Studies (GISS), United States	GISS Model E-R (GISS-ER) (1) 5.0° × 3.913°	GISS Model E, coupled with the Russell ocean model (GISS-E2-R) (1) 2.5° × 2.0°
Met Office Hadley Centre (MOHC), United Kingdom	Hadley Centre Coupled Model, version 3 (HadCM3) (1) 3.75° × 2.46575°; Hadley Centre Global Environment Model, version 1 (HadGEM1) (1) 1.875° × 1.25°	Hadley Centre Global Environment Model, version 2—Carbon Cycle (HadGEM2-CC) (1) 1.875° × 1.25°
Institute for Numerical Mathematics (INM), Russia	INM Coupled Model, version 3.0 (INM-CM3.0) (1) 5. 0° × 4.0°	INM Coupled Model, version 4.0 (INM-CM4.0) (1) 2.0° × 1.5°
Institut Pierre-Simon Laplace (IPSL) France	IPSL Coupled Model, version 4 (IPSL-CM4) (1) 3.75° × 2.5°	IPSL Coupled Model, version 5, coupled with NEMO, low resolution (IPSL-CM5A-LR) (4) 3.75° × 1.875°
Atmosphere and Ocean Research Institute (The University of Tokyo), National Institute for Environmental Studies, and Japan Agency for Marine-Earth Science and Technology, Model for Interdisciplinary Research on Climate (MIROC), Japan	MIROC, version 3.2 (MIROC3.2) (3) 2.8125° × 2.8125°	MIROC, version 5 (MIROC5) (3) 1.40625° × 1.40625°
Max Planck Institute for Meteorology (MPI-M), Germany	MPI-ECHAM5 (3) 1.875° × 1.875°	MPI Earth System Model, low resolution (MPI-ESM-LR) (3) 1.875° × 1.875°
Meteorological Research Institute (MRI), Japan	MRI Coupled Atmosphere–Ocean General Circulation Model, version 2.3.2a (MRI-CGCM2.3.2a) (5) 2.8125° × 2.8125°	MRI Coupled Atmosphere–Ocean General Circulation Model, version 3 (MRI-CGCM3) (1) 1.125° × 1.125°
National Center for Atmospheric Research (NCAR), United States	Community Climate System Model, version 3 (CCSM3) (4) 1.40625° × 1.40625°; Parallel Climate Model, version 1 (PCM1) (1)* 2.8125° × 2.8125°	Community Climate System Model, version 4 (CCSM4) (5) 1.25° × 0.9424°
Norwegian Climate Center (NCC), Norway		Norwegian Earth System Model, version 1 (intermediate resolution) (NorESM1-M) (1) 2.5° × 1.875°

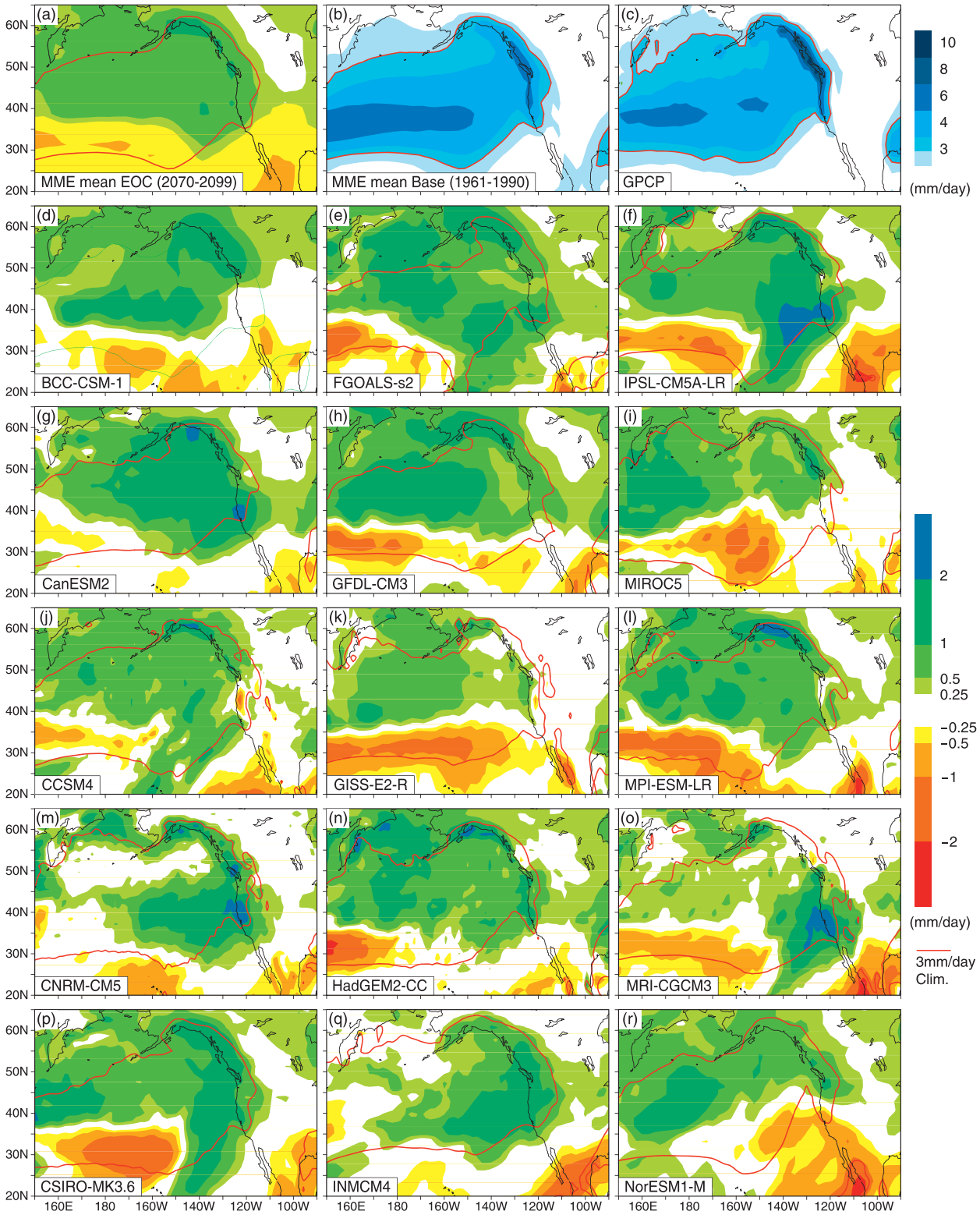

FIG. A1. (a) DJF precipitation change for the end of the century (2070–99 average) relative to the base period (1961–90) CMIP5 MME mean as in Fig. 1a, repeated for reference (the longitude range is slightly extended to permit individual model comparisons in the central Pacific). (b) CMIP5 MME mean base period (1961–90) precipitation climatology; the 3 mm day^{-1} contour of the climatology is highlighted in red. (c) GPCP observational precipitation climatology (1979–2005). (d)–(r) As in (a), but for each of the 15 models. The 3 mm day^{-1} contour from the each models climatology is superimposed. The upper color bar is for the climatology in (b),(c); the lower color bar is for all other panels.

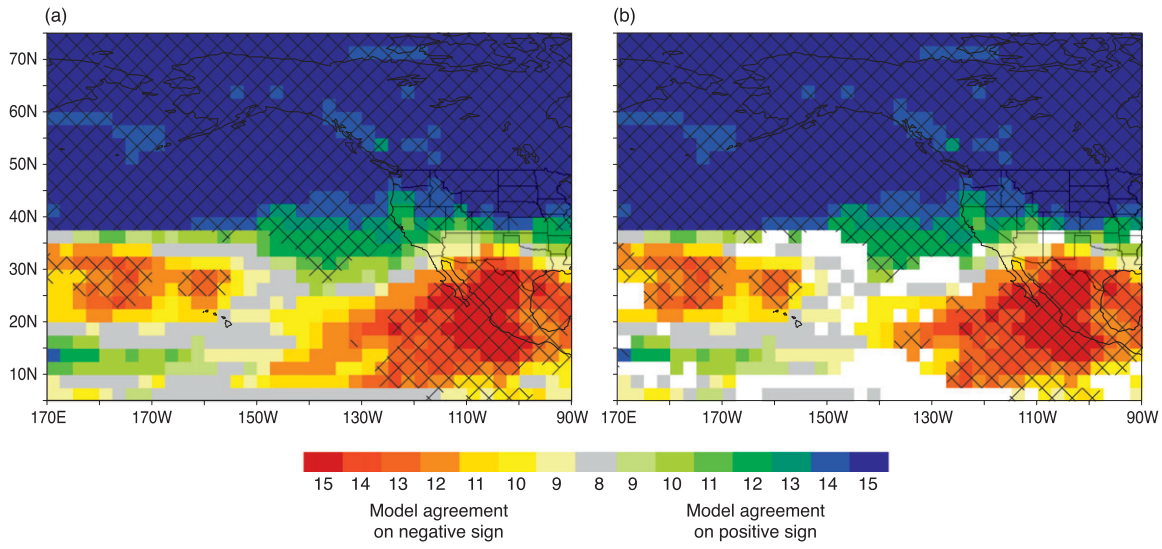

FIG. A2. Agreement on sign of DJF precipitation change (2070–99 minus 1961–90) for the CMIP5 ensemble as in Fig. 1b, but with criteria that combine agreement on sign with *t* tests on individual models: (a) Neelin et al. (2006) criteria and (b) Tebaldi et al. (2011) criteria. Cross-hatching in both figures indicates grid points that meet a combination of criteria for sign agreement and number of models passing a *t* test at a given level. Tebaldi et al. (2011) also include white shading where models exhibit the largest disagreement (see text for details).

Research Programme's Working Group on Coupled Modelling, which is responsible for CMIP, and we thank the climate modeling groups (listed in Table A1 of this paper) for producing and making available their model output. For CMIP the U.S. Department of Energy's Program for Climate Model Diagnosis and Intercomparison provides coordinating support and led development of software infrastructure in partnership with the Global Organization for Earth System Science Portals. GPCP data were provided by the NOAA/OAR/ESRL PSD, Boulder, Colorado, USA, from their Web site at http://www.esrl.noaa.gov/psd.

APPENDIX

Model Summary and Additional Figures for CMIP5 Models

The models referred to by their acronyms in the main text are listed in Table A1, noting also the number of available runs that went into the MME mean (e.g., in Figs. 1 and 2). Note that in Fig. 3 and Table A1 PCM1 is listed with NCAR in the CMIP3 models because it shares a version of an NCAR atmospheric model component.

The precipitation changes for the difference between 30-yr averages at end-of-century relative to base period for each model are shown in Fig. A1, along with MME mean change repeated for reference and the base period MME mean precipitation compared to the GPCP observational estimate. Figure A2 displays sign agreement for the CMIP5 ensemble (as in Fig. 1b), along with two ways of assessing the robustness for the end-of-century precipitation change. The two variants shown are criteria from either Neelin et al. (2006, hereafter N06; with significance levels adjusted) or Tebaldi et al. (2011, hereafter T11), shown as an overlay on Figs. A2a and A2b, respectively. For N06, grid points meet the criteria (shown as cross-hatching) where more than 50% of models *both* pass a two-tailed *t* test at the 95% confidence level *and* agree on the sign of change. For T11, cross-hatching indicates where more than 50% of models pass the *t* test at the 95% level and more than 80% of *those* models agree on sign. T11 also mask the grid points with more than 50% of models passing the *t* test at 95% but where fewer than 80% of them agree on sign, highlighting regions of model agreement not explained by sampling; these grid points are left unshaded in Fig. A2b. This aspect is fortunately not important for the storm-track extension or California precipitation signal. These criteria produce similar results for cross-hatching (T11 is essentially the same as N06 with adjusted thresholds in this respect) and there is a feature relevant to California that is worth noting. While the storm-track extension coming onto the coast passes these criteria, California land regions fall one model short. This is associated with the increased variance of DJF precipitation at the coast, which occurs to differing degrees in each model. This reinforces the caveats discussed in the text regarding interpreting the large-scale models too closely over the land regions and our preference for focusing on the

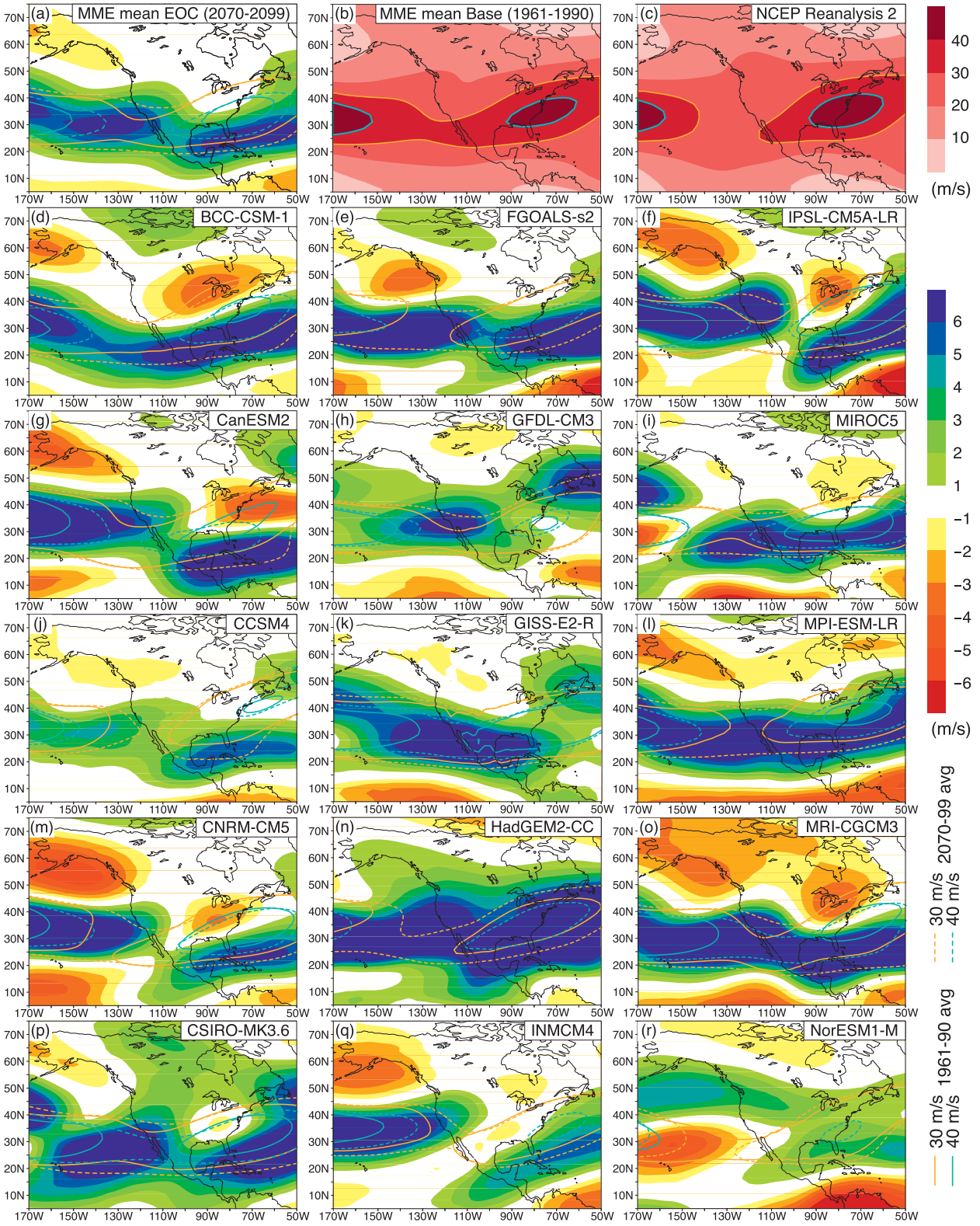

FIG. A3. As in Fig. A1, but for the 200-mbar zonal wind change (shading) for the end-of-century (2070–99 average) relative to a base period of 1961–90 under the RCP8.5 forcing scenario for the multimodel ensemble mean, as in Fig. 6a, repeated for reference. The 30 and 40 m s^{-1} contours of the DJF 200-mbar zonal wind are shown for the base period (solid contours) and the end-of-century period (dashed contours), respectively. (b) MME mean DJF 200-mbar zonal wind for the base period. (c) As in (b), but for NCEP Reanalysis 2 data for 1979–2005.

larger-scale feature leading onto the coast. However, these criteria have different aims than the significance tests discussed in the main text. The *t* test used in Fig. 1a tests whether the MME mean is significantly different from zero using the full ensemble. This can be done either by using the full set of time series of all model runs over the averaging periods or by averaging the time series and carrying out the test as for single realization (since the internal variability in the different runs can be considered independent, the statistic entering the *t* test has the same expected value). The binomial test in Fig. 1b likewise uses the full ensemble in rejecting the null hypothesis of equal probability of either sign. Langenbrunner and Neelin (2013) show in the case of ENSO teleconnections, for which the observed signal is available, that the N06 and T11 criteria omit substantial areas where the ensemble correctly predicts the sign of the observations.

Figure A3 shows the set of CMIP5 individual model results for the DJF 200-mbar zonal wind, as well as the MME mean end-of-century change, the MME mean climatology from the base period (1961–90) and the NCEP Reanalysis 2 climatology (averaged over 1979–2005 due to data availability). The 40 m s^{-1} contour in the CMIP5 climatology is an approximate agreement in latitude and eastward extent with that of NCEP, although the 30 m s^{-1} contour indicates that the jet weakens slightly more near the coast in the NCEP reanalysis. The corresponding CMIP3 climatological 200-mbar wind contours (Fig. 6b) are very similar to those of CMIP5.

REFERENCES

Adler, R. F., and Coauthors, 2003: The Version-2 Global Precipitation Climatology Project (GPCP) monthly precipitation analysis (1979–present). *J. Hydrometeor.,* **4,** 1147–1167.

Barnett, T. P., J. C. Adam, and D. P. Lettenmaier, 2005: Potential impacts of a warming climate on water availability in snow-dominated regions. *Nature,* **438,** 303–309.

——, and Coauthors, 2008: Human-induced changes in the hydrology of the western United States. *Science,* **319,** 1080–1083.

Caldwell, P., 2010: California wintertime precipitation bias in regional and global climate models. *J. Appl. Meteor. Climatol.,* **49,** 2147–2158.

Cayan, D. R., and J. O. Roads, 1984: Local relationships between United States West Coast precipitation and monthly mean circulation parameters. *Mon. Wea. Rev.,* **112,** 1276–1282.

——, K. T. Redmond, and L. G. Riddle, 1999: ENSO and hydrologic extremes in the western United States. *J. Climate,* **12,** 2881–2893.

——, E. P. Mauer, M. D. Dettinger, M. Tyree, and K. Hayhoe, 2008: Climate change scenarios for the California region. *Climatic Change,* **87,** S21–S42.

Chen, W. Y., and H. M. Van den Dool, 1997: Asymmetric impact of tropical SST anomalies on atmospheric internal variability over the North Pacific. *J. Atmos. Sci.,* **54,** 725–740.

Chou, C., and J. D. Neelin, 2004: Mechanisms of global warming impacts on regional tropical precipitation. *J. Climate,* **17,** 2688–2701.

——, ——, C.-A. Chen, and J.-Y. Tu, 2009: Evaluating the ''rich-get-richer'' mechanism in tropical precipitation change under global warming. *J. Climate,* **22,** 1982–2005.

Dettinger, M. D., D. R. Cayan, H. F. Diaz, and D. M. Meko, 1998: North–south precipitation patterns in western North America on interannual-to-decadal timescales. *J. Climate,* **11,** 3095–3111.

Duffy, P. B., and Coauthors, 2006: Simulations of present and future climates in the western United States with four nested regional climate models. *J. Climate,* **19,** 873–895.

Durack, P. J., S. E. Wijffels, and R. J. Matear, 2012: Ocean salinities reveal strong global water cycle intensification during 1950 to 2000. *Science,* **336,** 455–458, doi:10.1126/science.1212222.

Frierson, D. M. W., J. Lu, and G. Chen, 2007: Width of the Hadley cell in simple and comprehensive general circulation models. *Geophys. Res. Lett.,* **34,** L18804, doi:10.1029/2007gl031115.

Hayhoe, K., and Coauthors, 2004: Emissions pathways, climate change, and impacts on California. *Proc. Natl. Acad. Sci. USA,* **101,** 12 422–12 427.

Held, I. M., and B. J. Soden, 2006: Robust responses of the hydrological cycle to global warming. *J. Climate,* **19,** 5686–5699.

——, S. W. Lyons, and S. Nigam, 1989: Transients and the extratropical response to El Niño. *J. Atmos. Sci.,* **46,** 163–174.

Hsu, P.-C., and T. Li, 2012: Is ''rich-get-richer'' valid for Indian Ocean and Atlantic ITCZ? *Geophys. Res. Lett.,* **39,** L13705, doi:10.1029/2012GL052399.

Huffman, G. J., R. F. Adler, M. M. Morrissey, D. T. Bolvin, S. Curtis, R. Joyce, B. McGavock, and J. Susskind, 2001: Global precipitation at one-degree daily resolution from multisatellite observations. *J. Hydrometeor.,* **2,** 36–50.

Kim, J., 2005: A projection of the effects of the climate change induced by increased CO_2 on extreme hydrologic events in the western U.S. *Climatic Change,* **68,** 153–168.

Langenbrunner, B., and J. D. Neelin, 2013: Analyzing ENSO teleconnections in CMIP models as a measure of model fidelity in simulating precipitation. *J. Climate,* **26,** 4431–4446.

Leung, L.-R., Y. Qian, X. Bian, and A. Hunt, 2003: Hydroclimate of the western United States based on observations and regional climate simulation of 1981–2000. Part II: Mesoscale ENSO anomalies. *J. Climate,* **16,** 1912–1928.

Lorenz, D. J., and E. T. DeWeaver, 2007: Tropopause height and zonal wind response to global warming in the IPCC scenario integrations. *J. Geophys. Res.,* **112,** D10119, doi:10.1029/2006JD008087.

Lu, J., G. Chen, and D. M. W. Frierson, 2008: Response of the zonal mean atmospheric circulation to El Niño versus global warming. *J. Climate,* **21,** 5835–5851.

Matsuura, K., and C. J. Willmott, cited 2012: Terrestrial precipitation: 1900–2010 gridded monthly time series version 3.02. [Available online at http://climate.geog.udel.edu/~climate/.]

Mauer, E. P., 2007: Uncertainty in hydrologic impacts of climate change in the Sierra Nevada, California, under two emissions scenarios. *Climatic Change,* **82,** 309–325.

Meehl, G., and Coauthors, 2007: Global climate projections. *Climate Change 2007: The Physical Science Basis,* S. Solomon et al., Eds., Cambridge University Press, 747–845.

Moss, R. H., and Coauthors, 2010: The next generation of scenarios for climate change research and assessment. *Nature,* **463,** 747–756.

Mote, P. W., A. F. Hamlet, M. P. Clark, and D. P. Lettenmaier, 2005: Declining mountain snowpack in western North America. *Bull. Amer. Meteor. Soc.,* **86,** 39–49.

Murphy, J. M., B. B. B. Booth, M. Collins, G. R. Harris, D. M. H. Sexton, and M. J. Webb, 2007: A methodology for probabilistic

predictions of regional climate change from perturbed physics ensembles. *Philos. Trans. Roy. Soc. London,* **365A,** 1993–2028.

Neelin, J. D., M. Münnich, H. Su, J. E. Meyerson, and C. E. Holloway, 2006: Tropical drying trends in global warming models and observations. *Proc. Natl. Acad. Sci. USA,* **103,** 6110–6115.

Pierce, D. W., and Coauthors, 2013: Probabilistic estimates of future changes in California temperature and precipitation using statistical and dynamical downscaling. *Climate Dyn.,* **40,** 839–856, doi:10.1007/s00382-012-1337-9.

Redmond, K. T., and R. W. Koch, 1991: Surface climate and streamflow variability in the western United States and their relationship to large-scale circulation indices. *Water Resour. Res.,* **27,** 2381–2399.

Scheff, J., and D. Frierson, 2012: Twenty-first-century multimodel subtropical precipitation declines are mostly midlatitude shifts. *J. Climate,* **25,** 4330–4347.

Seager, R., N. Naik, and G. A. Vecchi, 2010: Thermodynamic and dynamic mechanisms for large-scale changes in the hydrological cycle in response to global warming. *J. Climate,* **23,** 4651–4668.

Straus, D. M., and J. Shukla, 1997: Variations of midlatitude transient dynamics associated with ENSO. *J. Atmos. Sci.,* **54,** 777–790.

Tebaldi, C., J. Arblaster, and R. Knutti, 2011: Mapping model agreement on future climate projections. *Geophys. Res. Lett.,* **38,** L23701, doi:10.1029/2011GL049863.

Trenberth, K. E., 2011: Changes in precipitation with climate change. *Climate Res.,* **47,** 123–138, doi:10.3354/cr00953.

——, and Coauthors, 2007: Observations: Surface and atmospheric climate change. *Climate Change 2007: The Physical Science Basis,* S. Solomon et al., Eds., Cambridge University Press, 235–336.

Xie, P., and P. A. Arkin, 1997: Global precipitation: A 17-year monthly analysis based on gauge observations, satellite estimates, and numerical model outputs. *Bull. Amer. Meteor. Soc.,* **78,** 2539–2558.

Yin, J. H., 2005: A consistent poleward shift of the storm tracks in simulations of 21st century climate. *Geophys. Res. Lett.,* **32,** L18701, doi:10.1029/2005GL023684.

Yin, X., A. Gruber, and P. Arkin, 2004: Comparison of the GPCP and CMAP merged gauge–satellite monthly precipitation products for the period 1979–2001. *J. Hydrometeor.,* **5,** 1207–1222.